

# Superconducting critical temperature of hole doped blue phosphorene

Davoud Nasr Esfahani<sup>1</sup> and Reza Asgari<sup>2,3</sup>

<sup>1</sup>Condensed Matter National Laboratory, Institute for Research in Fundamental Sciences (IPM), Tehran 19395-5531, Iran

<sup>2</sup>School of Physics, Institute for Research in Fundamental Sciences (IPM), Tehran 19395-5531, Iran

<sup>3</sup>School of Nano Science, Institute for Research in Fundamental Sciences (IPM), Tehran 19395-5531, Iran

(Dated: October 17, 2017)

We theoretically explore the superconducting critical temperature of hole doped blue phosphorene. Implementing the density functional theory calculations, we show that for the hole doped blue phosphorene, the isotropic superconducting state is induced owing to the quite strong electron-phonon coupling. The theory is based on the Migdal-Eliashberg formalism and the critical temperature is obtained through set-of-equations, self-consistency. In addition, we include a vertex correction diagram to the Migdal-Eliashberg formalism. The inclusion of the vertex correction beyond the Migdal-Eliashberg formalism changes the  $T_c$  about  $\pm 20K$ , depending on the level of the doping. Our accurate numerical results show that the superconducting critical temperature is still quite high, even in the cases that the vertex correction is implemented.

PACS numbers: 73.63.-b, 75.70.Cn, 85.75.-d, 73.43.Qt

## I. INTRODUCTION

Two-dimensional (2D) superconductivity has attracted much attention for the past decade and its explore has provided insight into a variety of rich physics occurs at the level of quantum phenomena. The fabrication of monolayer cuprate superconductors opens a new venue to investigate 2D materials and afterwards many new fabricated techniques such as molecular beam epitaxy together with the surface reconstruction process, mechanical exfoliation, and different methods for the production of field effect devices were introduced into the field of 2D superconductors [1]. Nowadays, researches can access superconductivity at the 2D limit in new advanced 2D crystalline materials.

In a 2D material with  $N$  layers, the Bardeen-Cooper-Schrieffer (BCS) theory [2] predicts that  $k_B T_c(N) = 1.13 E_D \exp(-1/(UN(\varepsilon_F)N))$  where  $N(\varepsilon_F)$  is the single layer density of states (DOS) at the Fermi energy,  $U$  is the pairing interaction strength and  $E_D$  is the Debay cutoff energy. Moreover, the critical field in a strictly 2D BCS superconductor is the Pauli paramagnetic limit,  $H_p = \Delta/(\sqrt{2}\mu_B)$  where  $\mu_B$  is the Bohr magneton and  $\Delta$  is the cooper pair energy gap. Above the Pauli field  $H_p$ , the Zeeman splitting of the Cooper pairs compensates the energy gained from creating the BCS condensate and therefore, 2D superconductivity is suppressed.

Black phosphorene (BP), a single layer analog of black phosphorus with puckered structure, has recently been exfoliated [3]. Tempted by successful synthesis of BP, several other monolayer structures have been proposed for phosphorus allotropes [4, 5]. Among them, blue phosphorene (BLP), which is a semiconductor with a buckled honeycomb structure and energy gap  $\sim 2eV$ , is energetically the most stable one after monolayer BP [4]. Moreover, it was shown that BLP is dynamically stable [6] and thermodynamically is more stable than BP in elevated temperatures [7]. Furthermore, BLP is recently realized through epitaxial growth [8]. In terms of applications, the BP has

been proposed as a high mobility material appropriate for a conventional field effect transistor applications [3]. On the other hand, it has been shown that the value of the mobility could be much smaller, in particular, owing to the anisotropy in the material and larger phase-space for the electron-phonon coupling (EPC) [9]. Later on, an EPC-mediated critical superconducting temperature  $T_c \sim 17K$  was reported for electron doped BP by using Lithium adsorption [10]. Its intercalation by several alkali metals (Li, K, Rb and Cs) has been described recently [11] and all the intercalated compounds have been found to be superconducting, exhibiting the same critical temperature of  $3.8 \pm 0.1K$  and practically identical characteristics in the superconducting state [11]. Furthermore, a superconducting temperature above 20K was recently predicted for electron doped bilayer-BLP through intercalation by alkali metals and alkaline earths.[12]

Early proposal for superconducting state in 2D materials refers to the electron doped graphene where the critical superconducting temperature is  $T_c \sim 15K$  and the electron doping was realized by Lithium adsorption on graphene [13–15]. However, recent experiments proposed new way of graphene superconductivity by activating the dormant potential for graphene in its own right by coupling it with a material called praseodymium cerium copper oxide [16]. Besides, 2D systems showing an electric-field-induced superconductivity [17].

In pristine graphene, there are at least two features which are detrimental to superconductivity at arbitrary low temperatures. First of all, the presence of the zero DOS at the Fermi level and second, the occurrence of a horizontal mirror plane ( $\sigma_h$  symmetry) in graphene. While the former is a prerequisite for the superconductivity, the latter only suppresses the EPC, i.e. the linear coupling to flexural modes is forbidden due to the symmetry considerations (the presence  $\sigma_h$  symmetry) [18, 19]. The role of the lithium adsorption on graphene is two folded. First, its role is to make a finite DOS at the Fermi energy and second, it promotes the coupling of the elec-

trons to flexural modes which leads to an enhanced the EPC [15, 20, 21].

Compared to graphene, since pristine BLP is an insulators, the electron/hole doping is necessary to induce a critical superconducting state. The required doping could be achieved by the electrical doping or by dopant or ad-atoms [22]. On the other hand, BLP has an inversion symmetry and  $\sigma_h$  does not hold, hence, it is expected that phonons with out-of-plane distortions are intrinsically coupled to the electrons and therefore no ad-atoms are necessary to promote the coupling to the out-of-plane distortions. The essence of the out-of-plane distortions could be understood by the fact that the majority of the states near the valence band maximum has  $p_z$  character.

In this paper, we carry out first-principles calculations to calculate the electron-phonon coupling of BLP to investigate the superconducting features of the system. Our theory is stemming from the multi-band Migdal-Eliashberg [23, 24] theory including the second-order self-energy as a vertex correction. Our numerical results show that a higher superconducting critical temperature occurs at lower hole density and thus the critical temperature ranging from 100 to 40K are obtained by considering the hole densities between  $5 \times 10^{13}$  to  $3.8 \times 10^{14}$   $\text{cm}^{-2}$ .

This paper is organized as follows. In Sec. II, we present the methodology used to calculate the superconducting state in the system and also describe second-order self-energy as a vertex correction. A set-of-equations is solved self-consistently to calculate the energy gap and critical temperature of the system. In Sec. III we present and describe main results of the superconducting state in the system and finally, we conclude and summarize our main results in Sec. IV

## II. THEORY AND DFT COMPUTATIONAL SIMULATIONS

In order to compute the electronic and phononic band dispersions of the system, the density functional theory (DFT) and density functional perturbation theory (DFPT) [25], as implemented in *Quantum Espresso* [26], are employed. The generalized gradient approximation in the scheme of Perdew, Burke, and Ernzerhof [27] and norm-conserving pseudopotentials are used throughout our calculations. Moreover, the Wannier interpolation of quantities (such as electron dispersions, phonon dispersions and electron-phonon interactions) from a fully self-consistent calculations on a coarse mesh to a fine mesh is applied as implemented in *EPW* code [28, 29], which is an integrated code into *Quantum Espresso*. In order to avoid interactions between layers along the  $z$  direction, a vacuum of 20 Å between layers is considered. Most of the results are examined between calculations within two different parameters set in some instances throughout this paper to provide increased precision for critical results and convergence check. These sets are namely DFT self-consistent calculations with integration over  $12 \times 12$

$k$ - Monkroost-Pack mesh, plane-wave energy cutoff of 70 Ry followed by DFPT calculation on a  $10 \times 10$   $q$ -mesh. The interpolation is performed on a  $10 \times 10$  (uniform coarse electronic)  $k$ -mesh and  $10 \times 10$  (uniform coarse phononic)  $q$ -mesh, and the second parameters set consists of the DFT self-consistent calculations with integration over  $20 \times 20$   $k$ - Monkroost-Pack, plane-wave energy cutoff of 90 Ry followed by DFPT calculation on a  $16 \times 16$   $q$ -mesh. The interpolation is performed on a  $16 \times 16$  (uniform coarse electronic)  $k$ -mesh and  $16 \times 16$  (uniform coarse phononic)  $q$ -mesh. No significant deviations between the two cases is observed. The results presented in the following are based on the latter set of parameters. Moreover, the Wannierisation (spin unpolarized) is performed using Wannier90 code [30] for the first 8 bands with an initial projection into S and P orbitals, and are checked with initial projections into  $\text{SP}^3$ . Furthermore, disentanglement procedure is employed and an upper bond for an inner window equal to 4.6 eV above the valance band maximum (VBM) is set, an average spread  $\sim 2.18$  Å<sup>2</sup>/per orbital was achieved. No imaginary part is observed for the real space representation of the resulting Hamiltonian.

We calculate the band structure and electronic DOS of BLP within two different approaches, i.e. a fully self-consistent calculation and Wannier interpolated bands. Our numerical results show that those results are in very good agreement and thus the results within the Wannier interpolation method are shown in Fig. 1. An indirect band gap about 1.9 eV is obtained between the VBM and the conduction band minimum (CBM) within the DFT simulations. In the following, we investigate BLP under the rigid shift of the Fermi energy deep into the lower energies below the VBM. Owing to the presence of a flatten band right near the VBM, the DOS shows a sharp peak. Notice that there is a discrepancy between the electronic band structure of BLP with that of monolayer phosphorene [31]. For the sake of completeness, in Fig. 1 we indicate two valence bands as band 4 and 5 labeled with red and green, respectively, for later purposes in order to understand the contribution of those bands on a superconducting quantity,  $\alpha^2F$ .

In Fig. 2, the projected DOS into  $p_x$ ,  $p_y$  and  $p_z$  is presented. Projected DOS is calculated on a Monkroost-Pack  $20 \times 20$   $k$ -mesh. Importantly enough, the states near the VBM has  $p_z$  character. Deeper into the energies and lower than the VBM, the flatness of the bands is suppressed which results in a sharp reduction of the DOS (see Fig. 1). This reduction in the DOS is mostly owing to the suppression of  $p_z$  states, where the contribution of the  $p_x + p_y$  is enhanced.

In Fig. 3 the phonon dispersion and phonon DOS of BLP are shown. The low-energy phonon modes are composed of three different bands, where two of them are characterized by the in-plane displacements at longer phonon wave lengths which are marked by longitudinal acoustic (LA) and transversal acoustic (TA) phonon modes, respectively. These modes acquire linear disper-

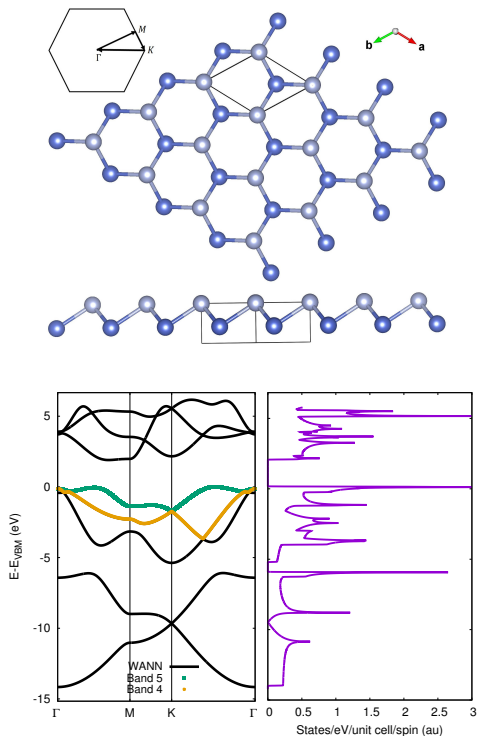


Figure 1. (Color online) The top and side views of the unit-cell of BLP and the  $k$ -path through high-symmetry points of the Brillouin zone. The band structure and DOS of BLP calculated within two different simulations, namely self-consistent calculation and Wannier interpolated band structure and they are essentially the same. An indirect bang gap around 1.9 eV is obtained. Two bands in the valence region indicate as band 4 and 5 for further purposes. Importantly, a flat feature of the band structure near the VBM results in a van Hove like peak at the vicinity of the VBM where  $E - E_{VBN} = -0.055$  eV.

sion at longer wavelengths with sound velocities. The other remaining mode has major out-of-plane displacement at longer wavelengths which is marked by ZA. This mode is softer than the other two modes and for a perfectly planar 2D material its energy dispersion acquires a  $\omega_{\mathbf{q}} \sim q^2$  relation. It is worth mentioning that in the BP the sound velocities in the  $\Gamma - Y$  direction calculated as 7.59 km/s and 4.48 km/s for LA and TA modes, respectively [31]. Along the  $\Gamma - X$  axis, on the other hand, the sound velocities obtained as 5.69 km/s and 5.27 km/s for longitudinal and transverse vibrations, respectively [31]. However, BLP acquires almost isotropic sound velocities along the  $\Gamma - M$  and  $\Gamma - K$  directions. The sound velocities in BLP are 8.3 km/s and 5.5 km/s for the longitudinal and transversal atomic motions, respectively. The longitudinal mode has a slightly greater velocity with respect to one reported in [6]. Moreover, the ZA mode in BP is different with respect of the BLP.

At the same time that the ZA modes have out-of-plane displacements for long wavelengths, however, for the BLP, the ZA mode acquires a tiny in-plane displacement as well, owing to its buckled nature. This small mixture be-

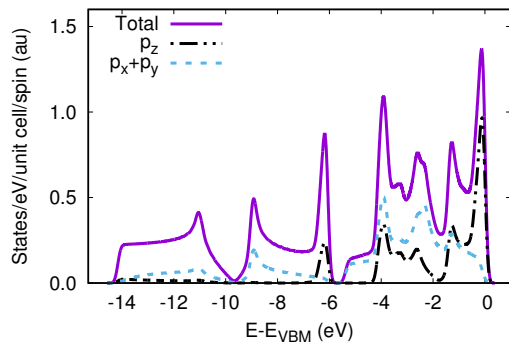


Figure 2. (Color online) Projected DOS, the states near the VBM illustrates  $p_z$  character, however, deeper into the valence band originates mainly from  $p_x + p_y$ .

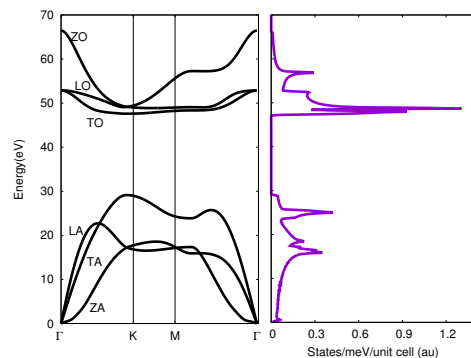


Figure 3. (Color online) The dispersion of the phonons and corresponding modes of BLP. In the low-energy, there are three different bands, two of these are characterized by the in-plane displacements (acoustic modes) at longer phonon wave lengths. The other remaining mode has major out-of-plane displacement at longer wavelengths. This mode is softer than the other two modes and for a perfectly planar 2D material its energy dispersion acquires a  $\sim q^2$  dispersion relation.

tween the in-plane and out-of-plane displacement results in a  $\beta_1 q + \beta_2 q^2$  dispersion for ZA mode at the long-wave lengths, where  $\beta_1$  is very tiny. In particular,  $\beta_1$  is very sensitive to the values of the energy cutoff and the method used for imposing the acoustic sum rule [32]. The higher energy phonons are composed of three branches of the out-of-phase displacements and are marked by transversal optical (TO), longitudinal optical (LO) modes for the modes with major in-plane displacements and ZO for the modes with major out-of-plane displacement. These two groups, i.e. optical and acoustic modes, are separated by a gap equal to  $\sim 17$  meV in phononic spectrum. Comparing the phonon dispersion with the phononic DOS in Fig. 3, we see that there are sharp peaks in the phononic DOS for which the dispersion shows flatten features as a function of phonon wavevector.

## A. Theory of superconductivity and Model

In normal state, the Landau Fermi liquid theory appears to work well. The Coulomb interactions give rise to a well-defined quasiparticle with a proper energy dispersion near the Fermi surface and they are assumed to exist. However, the phase transition to the superconducting state invalidates the perturbation approach. Nambu [33] showed how the formalism used in the normal state can be rewritten in such a way that the diagrams used to deal with the normal state are applicable for superconducting state.

In a system with  $N$  separated bands, one may extend the two-component spinor of the Nambu formalism to a  $2N$  component spinor and write the total Hamiltonian in the basis. To commence with, we first drop the Coulomb interaction in the Hamiltonian and consider a system incorporates the itinerant electrons, phonons and

the electron-phonon interactions. The reason to do so, is to explore the impact of different bands which are very close to the edge of the valence band maximum (see Fig. 1). Afterwards, we add the Coulomb interaction and many-body self-energies in the model. The spinor of the Nambu formalism is

$$\psi_{\mathbf{k}} = \begin{pmatrix} \vdots \\ c_{\mathbf{k}i\uparrow} \\ c_{-\mathbf{k}i\downarrow}^\dagger \\ \vdots \end{pmatrix} \quad (1)$$

where  $i = 1 \cdots N$  is the band index,  $c_{\mathbf{k}i\sigma}^\dagger$  ( $c_{\mathbf{k}i\sigma}$ ) is the creation (annihilation) operator for an electron in the band  $i$ , reciprocal vector  $\mathbf{k}$  and spin  $\sigma = \uparrow, \downarrow$ . The Hamiltonian of the system is given by,

$$\hat{H}_0 = \sum_{\mathbf{k}} \psi_{\mathbf{k}}^\dagger \hat{\varepsilon}_{\mathbf{k}} \hat{S} \psi_{\mathbf{k}} + \sum_{\mathbf{q}, \nu} \omega_{\mathbf{q}\nu} b_{\mathbf{q}, \nu}^\dagger b_{\mathbf{q}, \nu} + \sum_{\mathbf{k}\mathbf{q}\nu} (b_{\mathbf{k}-\mathbf{k}', \nu}^\dagger + b_{\mathbf{k}'-\mathbf{k}, \nu}) \psi_{\mathbf{k}'}^\dagger \hat{S} \hat{g}_{\mathbf{k}', \mathbf{k}}^\nu \psi_{\mathbf{k}} \quad (2)$$

where  $\hat{S}$ ,  $\hat{g}_{\mathbf{k}', \mathbf{k}}^\nu$  and  $\hat{\varepsilon}_{\mathbf{k}}$  are  $2N \times 2N$  matrices which elements of the  $\hat{S}$  satisfies  $\hat{S}_{ij} = (-1)^{i-1} \delta_{ij}$ , elements of the matrices  $\hat{g}_{\mathbf{k}', \mathbf{k}}^\nu$  and  $\hat{\varepsilon}_{\mathbf{k}}$  satisfy the following relations,

$$\begin{aligned} [\hat{g}_{\mathbf{k}, \mathbf{k}'}^\nu]_{2i-1, 2j-1} &= g_{\mathbf{k}i, \mathbf{k}'j}^{\nu\uparrow}, & [\hat{g}_{\mathbf{k}, \mathbf{k}'}^\nu]_{2i, 2j} &= g_{-\mathbf{k}i, -\mathbf{k}'j}^{\nu\downarrow} \\ [\hat{g}_{\mathbf{k}, \mathbf{k}'}^\nu]_{2i, 2j-1} &= 0, & [\hat{g}_{\mathbf{k}, \mathbf{k}'}^\nu]_{2i-1, 2j} &= 0 \\ [\hat{\varepsilon}_{\mathbf{k}}]_{2i-1, 2j-1} &= \delta_{ij} \varepsilon_{\mathbf{k}i\uparrow}, & [\hat{\varepsilon}_{\mathbf{k}}]_{2i, 2j} &= \delta_{ij} \varepsilon_{-\mathbf{k}i\downarrow} \\ [\hat{\varepsilon}_{\mathbf{k}}]_{2i-1, 2j} &= 0, & [\hat{\varepsilon}_{\mathbf{k}}]_{2i, 2j-1} &= 0 \end{aligned} \quad (3)$$

Here,  $i$  and  $j$  are band indexes,  $\hat{\varepsilon}_{\mathbf{k}}$  is the single-electron block energy relative to the Fermi level, with  $\varepsilon_{\mathbf{k}i\sigma} = \tilde{\varepsilon}_{\mathbf{k}i\sigma} - E_F$ , where  $\tilde{\varepsilon}_{\mathbf{k}i\sigma}$  is the energy dispersion which is extracted from DFT calculations. In the following we will represent the Fermi energy shift ( $\delta E_F$ ) corresponding to the VBM in the band structure calculation such that  $E_F = E_{VBM} + \delta E_F$ . Notice,  $\delta E_F$  is an input parameter which we use it for a rigid scan of the band structure and within the above mentioned definition of  $\varepsilon_{\mathbf{k}i\sigma}$  the chemical potential is readily set to zero.  $\hbar\omega_{\mathbf{q}, \nu}$  is the phonon energy of the wave vector  $\mathbf{q}$  and mode  $\nu$  and  $g_{\mathbf{k}i, \mathbf{k}'j}^{\nu\sigma}$  is electron-phonon matrix element (for the accurate definition of  $g_{\mathbf{k}i, \mathbf{k}'j}^{\nu\sigma}$  see Appendix. A).

By imposing the time reversal symmetry, we thus have  $g_{\mathbf{k}i, \mathbf{k}'j}^{\nu\uparrow} = g_{-\mathbf{k}i, -\mathbf{k}'j}^{\nu\downarrow} = g_{\mathbf{k}i, \mathbf{k}'j}^{\nu\downarrow}$  and  $\varepsilon_{\mathbf{k}i\uparrow} = \varepsilon_{-\mathbf{k}i\downarrow} = \varepsilon_{\mathbf{k}i}$ . Therefore, hereafter, we drop the spin index for the band dispersions and the electron-phonon couplings. The single-particle electronic Green's function is now a  $2N \times 2N$  matrix

$$\hat{G}(\mathbf{k}, \tau) = -\langle \mathcal{T}[\psi_{\mathbf{k}}(0) \psi_{\mathbf{k}}^\dagger(\tau)] \rangle \quad (4)$$

which its elements read as,

$$\begin{aligned} [\hat{G}(\mathbf{k}, \tau)]_{2i-1, 2j-1} &= -\langle \mathcal{T}[c_{\mathbf{k}i\uparrow}(\tau) c_{\mathbf{k}j\uparrow}^\dagger(0)] \rangle, \\ [\hat{G}(\mathbf{k}, \tau)]_{2i, 2j} &= -\langle \mathcal{T}[c_{-\mathbf{k}i\downarrow}(\tau) c_{-\mathbf{k}j\downarrow}^\dagger(0)] \rangle \\ [\hat{G}(\mathbf{k}, \tau)]_{2i-1, 2j} &= -\langle \mathcal{T}[c_{\mathbf{k}i\uparrow}(\tau) c_{-\mathbf{k}j\downarrow}^\dagger(0)] \rangle, \\ [\hat{G}(\mathbf{k}, \tau)]_{2i, 2j-1} &= -\langle \mathcal{T}[c_{-\mathbf{k}i\downarrow}(\tau) c_{\mathbf{k}j\uparrow}^\dagger(0)] \rangle \end{aligned} \quad (5)$$

where  $\mathcal{T}$  is time ordering on the imaginary time axis with  $-\beta < \tau < \beta$  where  $\beta$  is the inverse of temperature ( $k_B = 1$ ) and  $\langle \dots \rangle$  is grand canonical average. The Fourier components of the  $\hat{G}$  and  $D$ , where  $D$  refers to the single particle phonon Green's function, are expressed as

$$\begin{aligned} D_\nu(\mathbf{q}, \tau) &= \frac{1}{\beta} \sum_{n=-\infty}^{\infty} e^{-i\nu_n \tau} D_\nu(\mathbf{q}, i\nu_n) \\ \hat{G}(\mathbf{k}, \tau) &= \frac{1}{\beta} \sum_{n=-\infty}^{\infty} e^{-i\omega_n \tau} \hat{G}(\mathbf{k}, i\omega_n) \end{aligned} \quad (6)$$

where  $\nu_n = 2n\pi/\beta$ ,  $\omega_n = (2n+1)\pi/\beta$  with integer  $n$  are the Matsubara frequencies. Owing to the natural discretization of the Matsubara frequencies, it is more convenient to work with Matsubara frequencies.

The matrix representation of the noninteracting Green's function in the Matsubara frequency and reciprocal space representation takes the following form for the electrons

$$\hat{G}_0(\mathbf{k}, i\omega_n) = [i\omega_n \mathbb{1} - \hat{\varepsilon}_{\mathbf{k}} \hat{S}]^{-1} \quad (7)$$

and for the phonons

$$D_{0\nu}(\mathbf{q}, i\omega_n) = \frac{-2\omega_{\mathbf{q}, \nu}}{\omega_{\mathbf{q}, \nu}^2 + \omega_n^2} \quad (8)$$



Figure 4. The first-order self-energy diagram.

The fully interacting electron and phonon single particle Green's functions can be represented in terms of the non-interacting Green's function and the self-energy stem-

$$\hat{\Sigma}(\mathbf{k}, i\omega_n) = -T \int \frac{d\mathbf{k}'}{(2\pi)^2} \sum_{n'\nu} D_{0\nu}(\mathbf{k} - \mathbf{k}', i\omega_n - i\omega_{n'}) \hat{S} \hat{g}_{\mathbf{k};\mathbf{k}'}^\nu \hat{G}(\mathbf{k}', i\omega_{n'}) \hat{S} \hat{g}_{\mathbf{k}';\mathbf{k}}^\nu \quad (11)$$

where  $T$  is temperature and  $d\mathbf{k} \equiv d^2k$ . Apparently, the self-energy matrix is a  $2N \times 2N$  matrix as well. Carefully looking at the structure of the Green's function, one may represent it as a combination of the blocks of  $2 \times 2$  matrices which are labeled by combined band indexes  $i$  and

$$\hat{\Sigma}_i^{(1)}(\mathbf{k}, i\omega_n) = -T \sum_{\nu j n'} \int \frac{d\mathbf{k}'}{(2\pi)^2} D_{0\nu}(\mathbf{k} - \mathbf{k}', i\omega_n - i\omega_{n'}) |g_{\mathbf{k};\mathbf{k}'}^\nu|^2 \sigma_3 \hat{G}_j(\mathbf{k}', i\omega_{n'}) \sigma_3 \quad (12)$$

with,  $\sigma_3 = \begin{pmatrix} 1 & 0 \\ 0 & -1 \end{pmatrix}$ , in this way the non-interacting Green's function reads,

$$\hat{\mathbf{G}}_{0i}(\mathbf{k}, i\omega_n) = [i\omega_n \mathbb{1} - \varepsilon_{\mathbf{k}i} \sigma]^{-1} \quad (13)$$

### B. Isotropic approximation

In order to simplify the problem, we adopt the averaging procedure which has been applied to the single band case, and we only focus on quantities near the Fermi surface. To do so, we apply the averaging operator, i.e.  $\frac{1}{N_i(0)} \int \frac{d\mathbf{k}}{(2\pi)^2} \delta(\varepsilon_{\mathbf{k}i})$  (the averaging operator is band dependent and  $N_i(0)$  is the contribution of the band  $i$  to the total DOS at the Fermi energy such that  $N(0) = \sum N_i(0)$ ) on the both sides of the Eq. (12), which results in the following relation for the band-dependent

ming from the Dyson equation through

$$\hat{\mathbf{G}}^{-1}(\mathbf{k}, i\omega_n) = \hat{\mathbf{G}}_0^{-1}(\mathbf{k}, i\omega_n) - \hat{\Sigma}(\mathbf{k}, i\omega_n) \quad (9)$$

$$D_\nu^{-1}(\mathbf{q}, i\nu_n) = D_{0\nu}^{-1}(\mathbf{q}, i\nu_n) - \Gamma_\nu(\mathbf{q}, i\nu_n) \quad (10)$$

where  $\hat{\Sigma}$  and  $\Gamma$  are the electronic and the phononic self-energies.

Migdal's theorem [23] states that the vertex corrections to the electron self-energy are small, hence setting the full vertex to the bare one is a reasonable approximation. This particularly means that the interaction is truncated at order  $\sqrt{m/M} \sim \omega_D/\epsilon_F$ , with  $\omega_D$  is Debye frequency,  $\epsilon_F$  is Fermi energy,  $m$  and  $M$  are bare electron and ionic masses, respectively.

The self-energy is approximated by the first-order diagram (see Fig. 4) in the Dyson series as the rainbow or non-crossing diagram. The first order self-energy diagram given as follows

$j$ . Notice that like  $\hat{G}$  the self-energy matrix could be represented by a combination of blocks of  $2 \times 2$  matrices. Neglecting the inter-band contributions, the self-energy matrix will be block diagonal and could be represented by  $2 \times 2$  matrices which are labeled only by one band index, furthermore the  $\hat{S}$  matrix is replaced by  $\sigma_3$

self-energy,

$$\hat{\Sigma}_i^{(1)}(i\omega_n) = \frac{T}{N_i(0)} \sum_{\nu j n'} \int \frac{d\mathbf{k}d\mathbf{k}'}{(2\pi)^4} \frac{2\omega_{\mathbf{k}-\mathbf{k}',\nu}}{(\omega_n - \omega_{n'})^2 + \omega_{\mathbf{k}-\mathbf{k}',\nu}^2} \times \delta(\varepsilon_{\mathbf{k}i}) |g_{\mathbf{k};\mathbf{k}'}^\nu|^2 \sigma_3 \hat{\mathbf{G}}_j(\mathbf{k}', i\omega_{n'}) \sigma_3 \quad (14)$$

$$\text{where } \hat{\Sigma}_i(i\omega_n) = \langle \langle \hat{\Sigma}_i(\mathbf{k}, i\omega_n) \rangle \rangle_{FS} = \frac{1}{N_i(0)} \int \frac{d\mathbf{k}}{(2\pi)^2} \delta(\varepsilon_{\mathbf{k}i}) \hat{\Sigma}_i(\mathbf{k}, i\omega_n).$$

Further simplification could be achieved by applying the averaging operator in integration over  $\mathbf{k}'$  on the right-hand side of the Eq. (14), and further disentangling the integration over  $g_{\mathbf{k};\mathbf{k}'}^\nu$  and  $\hat{\mathbf{G}}_j(\mathbf{k}', i\omega_{n'})$ . Having used those



assumptions, the  $\mathbf{k}$ -independent self-energy now reads as,

$$\begin{aligned} \hat{\Sigma}_i^{(1)}(i\omega_n) &= \sum_{\nu j n'} \frac{T}{N_i(0)N_j(0)} \int \frac{d\mathbf{k}d\mathbf{k}'}{(2\pi)^4} \frac{2\omega_{\mathbf{k}-\mathbf{k}',\nu}}{(\omega_n - \omega_{n'})^2 + \omega_{\mathbf{k}-\mathbf{k}',\nu}^2} \\ &\times |g_{\mathbf{k}i,\mathbf{k}'j}^\nu|^2 \delta(\varepsilon_{\mathbf{k}i}) \delta(\varepsilon_{\mathbf{k}'j}) \int \frac{d\mathbf{k}'}{(2\pi)^2} \sigma_3 \hat{\mathbf{G}}_j(\mathbf{k}', i\omega_{n'}) \sigma_3 \end{aligned} \quad (15)$$

This treatment relies on the fact that  $g_{\mathbf{k}i,\mathbf{k}'j}^\nu$  variations

are smaller near the Fermi surface [34]. Therefore, it is replaced by its spherical average at the Fermi surface and large variations in the denominator of the  $\hat{\mathbf{G}}_j(\mathbf{k}', i\omega_{n'})$  as a function of  $\mathbf{k}'$  is treated exactly (see Eq. (17)). By rearranging Eq. (15), one may write down the following equation for the first-order self-energy

$$\hat{\Sigma}_i^{(1)}(i\omega_n) = T \sum_{j n'} \Lambda_{ij}(\omega_n - \omega_{n'}) \sigma_3 \hat{\mathbf{G}}_j(i\omega_{n'}) \sigma_3 \quad (16)$$

where  $\Lambda_{ij}$  and  $\hat{\mathbf{G}}_j(\omega_{n'})$  are defined as

$$\hat{\mathbf{G}}_j(i\omega_n) = \int \frac{d\mathbf{k}}{(2\pi)^2} \hat{\mathbf{G}}_j(\mathbf{k}, i\omega_n) = \int \frac{d\mathbf{k}}{(2\pi)^2} [i\omega_n \mathbb{1} - \varepsilon_{\mathbf{k}j} \sigma_3 - \hat{\Sigma}_j(i\omega_n)]^{-1} = \int d\varepsilon N_j(\varepsilon) [i\omega_n \mathbb{1} - \varepsilon \sigma_3 - \hat{\Sigma}_j(i\omega_n)]^{-1} \quad (17)$$

$$\Lambda_{ij}(\omega_n - \omega_{n'}) = \frac{1}{N_j(0)} \int d\Omega \frac{2\Omega \alpha^2 \mathbf{F}_{ij}(\Omega)}{(\omega_n - \omega_{n'})^2 + \Omega^2} \quad (18)$$

$$\alpha^2 \mathbf{F}_{ij}(\Omega) = \frac{1}{N_i(0)} \sum_{\nu} \int \frac{d\mathbf{k}}{(2\pi)^2} \frac{d\mathbf{k}'}{(2\pi)^2} |g_{\mathbf{k}i,\mathbf{k}'j}^\nu|^2 \delta(\varepsilon_{\mathbf{k}i}) \delta(\varepsilon_{\mathbf{k}'j}) \delta(\Omega - \omega_{\mathbf{k}-\mathbf{k}',\nu}) \quad (19)$$

while  $\alpha^2 \mathbf{F}_{ij}$  is not symmetric within the exchange of the indexes,  $\Lambda_{ij}$  is a symmetric function within the exchange of  $i$  and  $j$  indexes. Considering only the first-order diagram, i.e.  $\hat{\Sigma}_i(i\omega_n) = \hat{\Sigma}_i^{(1)}(i\omega_n)$ , the self-consistent solution of Eq. (16) with the Dyson equation (Eq. (9)) completes the solution of the Eliashberg equations. Furthermore, it is a common practice to parameterize the momentum averaged self-energy as,

$$\begin{aligned} \hat{\Sigma}_i(i\omega_n) &= i\omega_n [1 - Z_i(\omega_n)] \mathbb{1} + \chi_i(\omega_n) \sigma_3 \\ &+ \phi_i(\omega_n) \sigma_1 + \bar{\phi}_i(\omega_n) \sigma_2 \end{aligned} \quad (20)$$

where  $\sigma_1 = \begin{pmatrix} 0 & 1 \\ 1 & 0 \end{pmatrix}$ ,  $\sigma_2 = \begin{pmatrix} 0 & -i \\ i & 0 \end{pmatrix}$  and  $\mathbb{1}$  is a  $2 \times 2$  unit matrix. In the following, we choose a gauge such that  $\bar{\phi}_i(\omega_n) = 0$  [34]. By inserting the above mentioned decomposition for the local self-energy into the Dyson equation Eq. (9) and taking into account that  $\bar{\phi}_i(\omega_n) = 0$ ,  $\hat{\mathbf{G}}_i(\mathbf{k}, \omega_n)$  reads

$$\begin{aligned} \hat{\mathbf{G}}_i(\mathbf{k}, i\omega_n) &= - [i\omega_n Z_i(i\omega_n) \mathbb{1} + (\varepsilon_{\mathbf{k}} + \chi_i(i\omega_n)) \sigma_3 \\ &+ \phi_i(i\omega_n) \sigma_1] / \Theta_i(i\omega_n) \end{aligned} \quad (21)$$

with  $\Theta_i(i\omega_n) = (\omega_n Z_i(i\omega_n))^2 + (\varepsilon_{\mathbf{k}} + \chi_i(i\omega_n))^2 + \phi_i^2(i\omega_n)$ . By using the mentioned parametrization of  $\hat{\mathbf{G}}_i(\mathbf{k}, i\omega_n)$ , considering the definition of  $\hat{\mathbf{G}}_i(i\omega_n)$  and implying the DOS, which is a constant for the bands at the Fermi energy, one may calculate the integral over  $\varepsilon$  (in Eq. (17)) analytically. Performing the integration,  $\hat{\mathbf{G}}_i(i\omega_n)$  becomes

$$\begin{aligned} \hat{\mathbf{G}}_i(i\omega_n) &= -\pi N_i(0) \frac{[i\omega_n Z_i(i\omega_n) \mathbb{1} + \phi_i(i\omega_n) \sigma_1]}{\Xi_i(i\omega_n)} \\ \Xi_i(i\omega_n) &= \sqrt{[\omega_n Z_i(i\omega_n)]^2 + [\phi_i(i\omega_n)]^2} \end{aligned} \quad (22)$$

Inserting the above equation back to Eq. (16) and equating the corresponding elements of the matrices on both sides, the following set of equations for the components of the self-energy is achieved [35],

$$\begin{aligned} Z_i(i\omega_n) &= 1 + \frac{\pi T}{\omega_n} \sum_{j n'} \lambda_{ij}(\omega_n - \omega_{n'}) \frac{\omega_{n'} Z_j(i\omega_{n'})}{\Xi_j(i\omega_{n'})} \\ \phi_i(\omega_n) &= \pi T \sum_{j n'} \lambda_{ij}(\omega_n - \omega_{n'}) \frac{\phi_j(i\omega_{n'})}{\Xi_j(i\omega_{n'})} \end{aligned} \quad (23)$$

with  $\lambda_{ij}(\omega_n - \omega_{n'}) = N_j(0) \Lambda_{ij}(\omega_n - \omega_{n'})$ .

### C. Projected quantities

For the illustrative purposes, we compute the different projections of quantities like  $\alpha^2 \mathbf{F}$  and  $\mathbf{F}$ . We define the projected phonon DOS  $\mathbf{F}_\kappa(\omega)$  into the Cartesian coordinates  $\kappa$ , which represents the contribution of the phonons with polarization in the  $\kappa$  direction to the total phononic DOS. We consider only two major directions, an in-plane ( $\overline{xy}$ ) and out-of-plane ( $\overline{z}$ ),

$$\mathbf{F}_\kappa(\omega) = \sum_{\nu} \int \frac{d\mathbf{q}}{(2\pi)^2} \mathbf{P}_\kappa^{\nu\mathbf{q}} \delta(\omega - \omega_{\mathbf{q},\nu}) \quad (24)$$

where  $\kappa = \overline{xy}$  and  $\overline{z}$ ,  $\mathbf{P}_{\overline{xy}}^{\nu\mathbf{q}} = \sum_s \sum_{\kappa=x,y} \mathbf{e}^{\mathbf{q}\nu}_{s\kappa} \mathbf{e}^{\mathbf{q}\nu^*}_{s\kappa}$  and

$\mathbf{P}_{\overline{z}}^{\nu\mathbf{q}} = \sum_s \mathbf{e}_{s\overline{z}}^{\mathbf{q}\nu} \mathbf{e}_{s\overline{z}}^{\mathbf{q}\nu^*}$ ,  $s$  is the atomic index in the unit-cell, and  $\mathbf{e}^{\mathbf{q}\nu}_s$  is phonon polarization for branch  $\nu$  and vector  $\mathbf{q}$  (see Appendix A for the definition), and  $\mathbf{P}_\kappa^{\nu\mathbf{q}}$  satisfies  $\sum_{\kappa=\overline{xy},\overline{z}} \mathbf{P}_\kappa^{\nu\mathbf{q}} = 1$ .

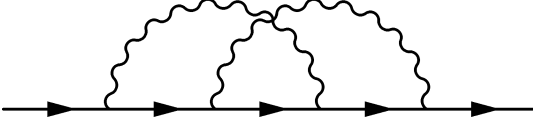


Figure 5. Correction of the second order self-energy in the electron-phonon interaction to the electron propagator.

The second projected quantity is projected  $\alpha^2\mathbf{F}$  into the Cartesian directions of the phonon displacements. The quantity is used to identify the contribution of the phonons with a specific character (here Cartesian displacement of phonons) in  $\alpha^2\mathbf{F}$  and therefore  $\lambda$ ,

$$\alpha^2\mathbf{F}_{ij}^{\kappa\kappa'}(\Omega) = \frac{1}{N_i(0)} \int \frac{d\mathbf{k}}{(2\pi)^2} \frac{d\mathbf{k}'}{(2\pi)^2} g_{\mathbf{k}i,\mathbf{k}'j}^{\nu\kappa} g_{\mathbf{k}i,\mathbf{k}'j}^{\nu\kappa'*} \times \delta(\varepsilon_{\mathbf{k}i})\delta(\varepsilon_{\mathbf{k}'j})\delta(\Omega - \omega_{\mathbf{k}-\mathbf{k}',\nu}) \quad (25)$$

$\kappa, \kappa' = \overline{xy}, \overline{z}$  and  $g_{\mathbf{k}i,\mathbf{k}'j}^{\nu\overline{xy}} = \sum_{\kappa=x,y} g_{\mathbf{k}i,\mathbf{k}'j}^{\nu\kappa}$  (for the definition of  $g_{\mathbf{k}i,\mathbf{k}'j}^{\nu\kappa}$  see Appendix A). Hence, we have the following relations between the projected  $\alpha^2\mathbf{F}$ s as

$$\alpha^2\mathbf{F}_{ij}(\Omega) = \sum_{\kappa,\kappa'=\overline{xy},\overline{z}} \alpha^2\mathbf{F}_{ij}^{\kappa\kappa'}(\Omega) \quad (26)$$

$$\alpha^2\mathbf{F}^{\kappa\kappa'}(\Omega) = \frac{1}{N(0)} \sum_{ij} N_i(0) \alpha^2\mathbf{F}_{ij}^{\kappa\kappa'}(\Omega) \quad (27)$$

$$(28)$$

$\psi_{\mathbf{k}} = \begin{pmatrix} c_{\mathbf{k}\uparrow} \\ c_{-\mathbf{k}\downarrow}^\dagger \end{pmatrix}$ ,  $c_{\mathbf{k}\sigma}$  ( $c_{\mathbf{k}\sigma}^\dagger$ ) annihilates (creates) electrons in band 5, reciprocal vector  $\mathbf{k}$  and spin  $\sigma$ .  $\langle \mathbf{k}_3\mathbf{k}_4|V_C|\mathbf{k}_1\mathbf{k}_2\rangle$  is the bare electron-electron Coulomb interaction, the translational invariance of  $V_c$  restricts  $\mathbf{k}_1 + \mathbf{k}_2 - \mathbf{k}_3 - \mathbf{k}_4$  being zero or a reciprocal lattice vector  $\mathbf{K}$ . Considering the above Coulomb contribution to  $\hat{\mathcal{H}}_0$  and neglecting the contribution of the other bands, one may write the isotropic first order self-energy as follows,

$$\hat{\Sigma}^{(1)}(i\omega_n) = T \sum_{n'} \{ \Lambda(\omega_n - \omega_{n'}) - \bar{V}_C \} \sigma_3 \hat{\mathbf{G}}^{od}(i\omega_{n'}) \sigma_3 \quad (32)$$

$$\text{with } \bar{V}_C = \frac{1}{N(0)^2} \int \frac{d\mathbf{k}}{(2\pi)^2} \frac{d\mathbf{k}'}{(2\pi)^2} V_C(\mathbf{k} - \mathbf{k}') \delta(\varepsilon_{\mathbf{k}'}) \delta(\varepsilon_{\mathbf{k}}),$$

The total  $\alpha^2\mathbf{F}$  reads

$$\alpha^2\mathbf{F}(\Omega) = \frac{1}{N(0)} \sum_{ij} N_i(0) \alpha^2\mathbf{F}_{ij}(\Omega) \quad (29)$$

The band projected mass renormalization factor is defined as

$$\lambda_{ij} = 2 \int d\Omega \frac{\alpha^2\mathbf{F}_{ij}(\Omega)}{\Omega} \quad (30)$$

the relation between total  $\lambda$  and  $\lambda_{ij}$  is  $\lambda = \frac{1}{N(0)} \sum_{ij} N_i(0) \lambda_{ij}$ .

#### D. Coulomb Interaction contribution

In the following, we only focus on the band with the largest contribution on  $\alpha^2\mathbf{F}$  (we will show that the main contribution comes from band 5, where band 5 is marked with green color in Fig. 1). The justification of this assumption is based on the fact that the contribution of band 4 in  $\alpha^2\mathbf{F}$  is negligible in comparison to that from band 5 for the largest Fermi energy shift (see Fig. 9 in numerical section) and the other lower bands acquire vanishing  $\alpha^2\mathbf{F}$  for all examined  $\delta E_F$  (not shown here). Therefore, we only consider band 5 and for the sake of simplicity, we neglect band indexing regarding band structure, Green's function and self-energies.

The Hamiltonian corresponding to the electron-electron interaction has the following form [36, 37],

$$\hat{\mathcal{H}}_c = \frac{1}{2} \sum_{\mathbf{k}_1\mathbf{k}_2\mathbf{k}_3\mathbf{k}_4} \langle \mathbf{k}_3\mathbf{k}_4|V_C|\mathbf{k}_1\mathbf{k}_2\rangle \psi_{\mathbf{k}_3}^\dagger \sigma_3 \psi_{\mathbf{k}_1} \times \psi_{\mathbf{k}_4}^\dagger \sigma_3 \psi_{\mathbf{k}_2} \quad (31)$$

$\Lambda(\omega_n - \omega_{n'}) = \frac{1}{N_5(0)} \int d\Omega \frac{2\Omega \alpha^2\mathbf{F}_{55}(\Omega)}{(\omega_n - \omega_{n'})^2 + \Omega^2}$ , and  $\hat{\mathbf{G}}^{od}$  holds for off-diagonal part of the Green's function. The reason of holding only the off-diagonal part of Green's function is the fact that the electron-electron interaction has already been considered for diagonal parts in DFT calculation of the electronic band structure [34]. By imposing the constant DOS approximation, the isotropic Eliashberg equations have the following form

$$\begin{aligned} \omega_n [1 - Z(i\omega_n)] &= -\pi T \sum_{n'} N(0) \Lambda(\omega_n - \omega_{n'}) \frac{\omega_{n'} Z(i\omega_{n'})}{\Xi(i\omega_{n'})} \\ \phi(i\omega_n) &= \pi T \sum_{n'} [N(0) \Lambda(\omega_n - \omega_{n'}) - N(0) \bar{V}_c] \frac{\phi(i\omega_{n'})}{\Xi(i\omega_{n'})} \end{aligned} \quad (33)$$

In spite of the electron-phonon interaction kernel, the

$\bar{V}_C$  does not have any natural upper cutoff in energy summation in Eq. (33). However, owing to retardation effects, the repulsion felt by the electrons is smaller than instantaneous interactions. The procedure of the scaling of the Coulomb interaction is to replace the  $\mu_c = N(0)\bar{V}_C$  with the well-known Morel-Anderson pseudopotential  $\mu_c^* = \frac{\mu_c}{1 + \mu_c \ln(E/\omega_D)}$  with  $E$  is the electronic bandwidth and  $\omega_D$  is the phonon energy scale which is as order of Debye energy [38–41]. These retardation effects are still operative for larger interactions and where higher order corrections are necessary, although they are less efficient due to the reduction in bandwidth [42]. Furthermore, retardation effects impose an upper energy cutoff for  $\mu_c^*$  in energy summation [41] in Eq. (33). Eventually, by considering the above mentioned retardation effects of electron-electron interaction, one may rewrite Eq. (33) as

$$\begin{aligned} Z(i\omega_n) &= 1 + \frac{\pi T}{\omega_n} \sum_{n'} \lambda(\omega_n - \omega_{n'}) \frac{\omega_{n'} Z(i\omega_{n'})}{\Xi(i\omega_{n'})} \\ \phi(i\omega_n) &= \pi T \times \sum_{n'} [\lambda(\omega_n - \omega_{n'}) - \mu_c^* \Theta(\omega_c - |\omega_{n'}|)] \frac{\phi(i\omega_{n'})}{\Xi(i\omega_{n'})} \end{aligned} \quad (34)$$

with  $\lambda(\omega_n - \omega_{n'}) = N(0)\Lambda(\omega_n - \omega_{n'})$ ,  $\Theta(x)$  is the Heaviside step function and  $\omega_c \sim 5 - 10 \omega_D$ . In order to achieve a common ground for comparison between the constant DOS approximation and that of variable DOS at the Fermi energy, in analogy with the constant DOS approximation, one may express Eq. (32) as

$$\begin{aligned} \hat{\Sigma}^{(1)}(i\omega_n) &= T \sum_{n'} \{ \Lambda(\omega_n - \omega_{n'}) \sigma_3 \hat{\mathbf{G}}(i\omega_{n'}) \sigma_3 \\ &\quad - \frac{\mu_c^*}{N(0)} \Theta(|\omega_{n'}| - \omega_c) \sigma_3 \hat{\mathbf{G}}^{od}(i\omega_{n'}) \sigma_3 \} \end{aligned} \quad (35)$$

$$\begin{aligned} \hat{\mathcal{H}} &= \sum_{\mathbf{k}} \varepsilon_{\mathbf{k}} \psi_{\mathbf{k}}^\dagger \sigma_3 \psi_{\mathbf{k}} + \sum_{\nu=1,2} \sum_{\mathbf{q}} \omega_\nu b_{\mathbf{q},\nu}^\dagger b_{\mathbf{q},\nu} + \sum_{\nu=1,2} \sum_{\mathbf{k},\mathbf{q}} g_\nu (b_{\mathbf{q},\nu}^\dagger + b_{-\mathbf{q},\nu}) \psi_{\mathbf{k}+\mathbf{q}}^\dagger \sigma_3 \psi_{\mathbf{k}} \\ &\quad + \frac{1}{2} \sum_{\mathbf{k}_1 \mathbf{k}_2 \mathbf{k}_3 \mathbf{k}_4} \langle \mathbf{k}_3 \mathbf{k}_4 | V_C | \mathbf{k}_1 \mathbf{k}_2 \rangle \psi_{\mathbf{k}_3}^\dagger \sigma_3 \psi_{\mathbf{k}_1} \times \psi_{\mathbf{k}_4}^\dagger \sigma_3 \psi_{\mathbf{k}_2} \end{aligned} \quad (36)$$

where  $\varepsilon_{\mathbf{k}}$  is the energy dispersion of band 5 relative to  $E_F$ ,  $\omega_\nu$  is the phonon energy and  $g_\nu$  is the corresponding electron-phonon interaction. The interaction kernel of this model can be written as  $\tilde{\Lambda}(\omega_n - \omega_{n'}) = \sum_{\nu} \frac{2\omega_\nu g_\nu^2}{(\omega_n - \omega_{n'})^2 + \omega_\nu^2}$ . In the next step, we fit the kernel of the new system with that of the original system. Happily,

Clearly, by using constant DOS approximation for Eq. (35) together with Dyson equation, one finds Eqs. (34).

## E. Second-order self-energy: Vertex corrections

When there is a flat band near the VBM (as is the case for us corresponding to the electronic structure of the BLP, see Fig. 1), the first-order self-energy might not be accurate enough to explore the physics of the system. In this case, we should include the second-order self-energy considering the vertex corrections [43]. In addition, since we incorporate all electron-electron contributions in the electron Green's function, therefore, we will just consider the vertex correction on the electron-phonon interaction. To proceed, we impose further simplifications to overcome difficulties owing to the computational complexity of the problem. Therefore, by using the calculated  $\alpha^2 \mathbf{F}$  for each Fermi energy shift, we derive an effective Hamiltonian such that the interaction kernel of the isotropic averaged interaction kernel is the same as the interaction kernel of the newly constructed Hamiltonian. In this regard, we consider a simple Holstein model composed of the two dispersionless Einstein modes. Furthermore, we consider a model which has the same electronic band structure as the band structure of band 5,

we find that the kernel of the system with two phonon modes fits with great accuracy to the kernel of the original model. In order to include vertex corrections, therefore, we evaluate the second crossing self-energy diagram (see Fig. 5) like as,

$$\begin{aligned} \hat{\Sigma}^{(2)}(\mathbf{k}, i\omega_n) &= (-T)^2 \sum_{\omega_{n_1}, \omega_{n_2}} \int \frac{d\mathbf{q}}{(2\pi)^2} \frac{d\mathbf{q}'}{(2\pi)^2} \sigma_3 \hat{\mathbf{G}}(\mathbf{k} - \mathbf{q}, i\omega_{n_1}) \sigma_3 \hat{\mathbf{G}}(\mathbf{k} - \mathbf{q} - \mathbf{q}', i\omega_{n_2}) \\ &\quad \times \sigma_3 \hat{\mathbf{G}}(\mathbf{k} - \mathbf{q}', i\omega_n - i\omega_{n_1} + i\omega_{n_2}) \sigma_3 \Lambda(\omega_n - \omega_{n_1}) \Lambda(\omega_{n_1} - \omega_{n_2}) \end{aligned} \quad (37)$$



By averaging over the Fermi surface, the self energy is given by

$$\hat{\Sigma}^{(2)}(i\omega_n) = \frac{(-T)^2}{N(0)} \sum_{\omega_{n_1}, \omega_{n_2}} \int \frac{d\mathbf{k}}{(2\pi)^2} \frac{d\mathbf{q}}{(2\pi)^2} \frac{d\mathbf{q}'}{(2\pi)^2} \delta(\varepsilon_{\mathbf{k}}) \sigma_3 \hat{\mathbf{G}}(\mathbf{k} - \mathbf{q}, i\omega_{n_1}) \sigma_3 \hat{\mathbf{G}}(\mathbf{k} - \mathbf{q} - \mathbf{q}', i\omega_{n_2}) \times \sigma_3 \hat{\mathbf{G}}(\mathbf{k} - \mathbf{q}', i\omega_n - i\omega_{n_1} + i\omega_{n_2}) \sigma_3 \Lambda(\omega_n - \omega_{n_1}) \Lambda(\omega_{n_1} - \omega_{n_2}) \quad (38)$$

The evaluation of the Eq. (38) has a computational complexity as order of  $O(N^6)$  regarding reciprocal integration, where  $N$  is the number of mesh points in each direction of the reciprocal space. To reduce the complexity, it is more efficient to evaluate the diagram in the real space. To perform the evaluation of the Eq. (38), we use the real space representation of the second order-diagram followed by a backward Fourier transformation on the real-space diagram. The real-space diagram can be evaluated as follows

$$\hat{\Sigma}^{(2)}(\mathbf{x}, i\omega_n) = (-T)^2 \sum_{\omega_{n_1}, \omega_{n_2}} \sigma_3 \hat{\mathbf{G}}(\mathbf{x}, i\omega_{n_1}) \sigma_3 \hat{\mathbf{G}}(-\mathbf{x}, i\omega_{n_2}) \sigma_3 \times \hat{\mathbf{G}}(\mathbf{x}, i\omega_n - i\omega_{n_1} + i\omega_{n_2}) \sigma_3 \Lambda(\omega_n - \omega_{n_1}) \Lambda(\omega_{n_1} - \omega_{n_2}) \quad (39)$$

where  $\hat{\mathbf{G}}(\mathbf{x}, i\omega_n) = \int \frac{d\mathbf{k}}{(2\pi)^2} e^{-i\mathbf{x}\cdot\mathbf{k}} \hat{\mathbf{G}}(\mathbf{k}, i\omega_n)$  and the second-order self-energy is

$$\hat{\Sigma}^{(2)}(i\omega_n) = \frac{1}{N(0)} \int \frac{d\mathbf{k}}{(2\pi)^2} \delta(\varepsilon_{\mathbf{k}}) \hat{\Sigma}^{(2)}(\mathbf{k}, i\omega_n) \quad (40)$$

with  $\hat{\Sigma}^{(2)}(\mathbf{k}, i\omega_n) = \sum_{\mathbf{x}} e^{i\mathbf{k}\cdot\mathbf{x}} \hat{\Sigma}^{(2)}(\mathbf{x}, i\omega_n)$ . Having calculated the first-and second-order self-energy, the total self-energy is thus given by

$$\hat{\Sigma}(i\omega_n) = \hat{\Sigma}^{(1)}(i\omega_n) + \hat{\Sigma}^{(2)}(i\omega_n) \quad (41)$$

As usual, a self-consistency must be imposed between Eq. (41) and Dyson equation, Eq. (9).

### III. NUMERICAL RESULTS

In this section we mainly consider the Migdal-Eliashberg formalism considering the first-order self-energy. Eventually, we also include the vertex correction to the self-energy and only discuss the superconducting energy gap and critical temperature as well. We define  $\varepsilon_{\mathbf{k}} = \tilde{\varepsilon}_{\mathbf{k}} - E_F$ , where  $\tilde{\varepsilon}_{\mathbf{k}}$  is the energy dispersion, which is extracted from DFT calculations. Once again, we investigate BLP under the rigid shift of the Fermi energy deep into the lower energies below the VBM. In particular, our analysis is based on  $\delta E_F = -0.02, -0.055, -0.105, -0.155$  and  $-0.205$  eV. The corresponding hole densities are  $\rho_h = 5.0 \times 10^{13}, 1.5 \times 10^{14}, 2.4 \times 10^{14}, 3.1 \times 10^{14}$  and  $3.8 \times 10^{14}$  cm $^{-2}$ , respectively, with  $\rho_h(E_F) = [N_{tot} - \int_{-\infty}^{E_F} N(\varepsilon) d\varepsilon]/S$ , where  $N(\varepsilon)$  is the DOS,  $S$  is the unit-cell surface area and  $N_{tot}$  is the total holes in the valence band when  $E_F = E_{VBM}$ .

The interpolation is performed for a range of fine meshes. In most critical cases, we use a fine  $800 \times 800$   $k$ -mesh and  $200 \times 200$   $q$ -mesh, whereas in less critical cases, we use  $200 \times 200$   $k$ -mesh and  $200 \times 200$   $q$ -mesh. The delta functions are approximated by a Gaussian function as  $\delta(x) \sim \frac{1}{\sqrt{\pi}\sigma} e^{-x^2/\sigma^2}$  for calculating the  $\alpha^2\mathbf{F}$  and  $\lambda$ . The convergence of the quantities is thoroughly checked for a range of  $\sigma$ ,  $k$ - and  $q$ -meshes (see Appendix B). Particularly, the DOS,  $\alpha^2\mathbf{F}$  and  $\lambda$  are insensitive to the electronic broadening for a range  $\sigma = 0.00125 - 0.01$  eV and the phononic broadening is set to be  $\sigma_{ph} = 0.1$  meV. Furthermore, due to the small energy scale of the out-of-plane acoustic mode, inaccuracies are inevitable. In order to filter numerical inaccuracies out, for actual calculations of  $\lambda$  and solutions of the Eliashberg equations a lower cutoff  $\sim 1$  MeV was considered such that below this cutoff the  $\alpha^2\mathbf{F}$  is omitted. To further reduce the numerical complexity of the evaluation of Eq. (39), we employ the observation that Green's function is a quiet local in real space, therefore, an upper real-space cutoff over which the  $\hat{\Sigma}^{(2)}(\mathbf{x}, i\omega_n)$  was set to zero, is considered. Here, we use a cutoff of 20 sites for each direction. Moreover, while for the evaluation of the Eq. (39) we use  $\alpha^2\mathbf{F}$  resulting from finest mesh available, all the vertex corrections are performed on a  $200 \times 200$   $k$ -mesh with  $\sigma = 0.01$  EV and the upper cutoff in frequency summation  $\omega_c = 0.5$  eV.

Fig. 6 depicts the total  $\alpha^2\mathbf{F}$  for different rigid shift of the Fermi energy,  $\delta E_F = -0.02$  and  $-0.205$  eV, deep into the valence states. Apparently for the larger shift,  $\alpha^2\mathbf{F}$  suffers from a dramatic reduction in its magnitude.

As it is obvious from the inset of Fig. 6, the total unit-less coupling,  $\lambda$ , shows a dramatic decreasing as a function of  $\delta E_F$ . Looking at the form of the  $\alpha^2\mathbf{F}$  (see Eq. (29)), it is expected that by reducing the DOS, the  $\lambda$  decreases as well. This could be qualitatively attributed by considering a dispersion-less phonon spectrum.  $\lambda$  can be evaluated as  $\lambda = 2N(0)\tilde{g}^2/\omega_0$ , where  $\omega_0$  and  $\tilde{g}$  are the effective dispersion-less phonon energy and electron-phonon interaction for each Fermi energy shift and  $N(0)$  is the DOS at the Fermi energy. Therefore, a reduction in the DOS induces a decreasing in the  $\lambda$  as long as  $\tilde{g}$  is a constant as a function of the  $\delta E_F$ .

In order to disentangle the share of the  $N(0)$  and  $\tilde{g}$  for different  $\lambda$  as a function of  $\delta E_F$ , in Fig. 7(a), we plot  $\lambda/\lambda_{\max}$  and  $N(0)/N(0)_{\max}$  as a function of  $\delta E_F$ . By moving into the valence band states, both  $\lambda$  and  $N(0)$  decrease as a function of the  $\delta E_F$ , however, the rate of the decreasing in  $\lambda$  is larger than that of the  $N(0)$  when they are compared with the  $\lambda_{\max}$  and  $N(0)_{\max}$ ,

where generally it is the signature of the suppression of the electron-phonon interactions. Therefore, we plot  $\sqrt{\langle g^2 \rangle}$  as a function of the  $\delta E_F$  in Fig. 7(b), where  $\langle g^2 \rangle = \frac{1}{N(0)} \int \alpha^2 \mathbf{F}(\Omega) d\Omega$ . By moving into the valence band states, the value of the  $\sqrt{\langle g^2 \rangle}$  suppresses. Hence, the reduction in the unit-less electron-phonon coupling as a function of the  $\delta E_F$  is not only owing to the suppression of the DOS at the Fermi energy, but also the electron-phonon interaction is generally suppressed when one changes  $E_F$  deeper into the valence bands.

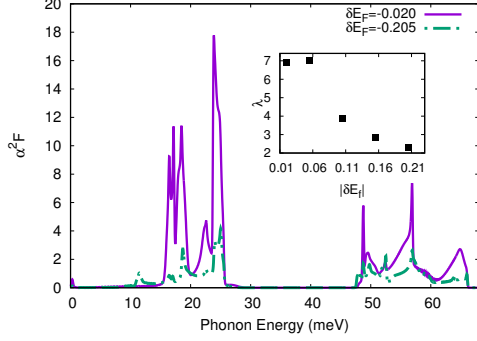


Figure 6. (Color online) Total  $\alpha^2 \mathbf{F}$  as a function of the rigid shift of the Fermi energy for different values of  $\delta E_F = -0.02$  and  $-0.205$  eV. Notice that in the case of the large shifts, total  $\alpha^2 \mathbf{F}$  suffers from a dramatic reduction in its magnitude since a reduction in the DOS induces a decreasing in the  $\lambda$ . Inset:  $\lambda$  as a function of the rigid shift of the Fermi energy for different values of  $\delta E_F$ .

In order to observe which character of the system is responsible for a behavior of the  $\lambda$  as a function of the  $\delta E_F$ , we look at the projected  $\alpha^2 \mathbf{F}$  into Cartesian directions

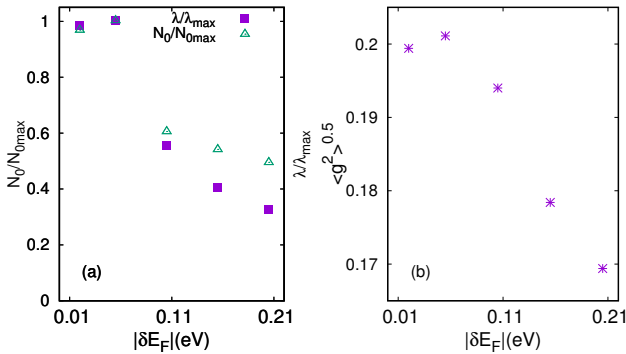


Figure 7. (Color online) (a)  $\lambda/\lambda_{\max}$ ,  $N(0)/N(0)_{\max}$  and (b)  $\sqrt{\langle g^2 \rangle}$  as a function of  $\delta E_F = -0.02, -0.055, -0.105, -0.155$  and  $-0.205$  eV. Upon larger  $\delta E_F$  both  $\lambda_{\max}$  and  $N(0)$  decrease but the faster decrease is obvious for  $\lambda$ , which is the signature of the decreasing in averaged electron-phonon interaction (see part (b) of the figure).

of the phonon displacements. The quantities are already defined in Sec. II C. We consider two major projection directions, i.e.  $\kappa, \kappa' = \overline{xy}, \overline{z}$ .

In Fig. 8(a) the projected  $\alpha^2 \mathbf{F}^{\kappa\kappa'}$  as a function of phonon energy for  $\delta E_F = -0.055$  eV is presented for different projection directions. It is seen that the electrons mainly couple to the deformations which are induced by the out-of-plane displacements of the phonons. Comparing with the projected phonon DOS in Fig. 8(c), it is possible to observe that the presence of the phonons with considerable out-of-plane character is a quantity to acquire sizable  $\alpha^2 \mathbf{F}$ . In particular, by noticing at the lower edge of the optical phonon spectrum, around 48 meV which is indicated by an arrow in Fig. 8(c), one may observe a large peak with in-plane character, however, there is no significant  $\alpha^2 \mathbf{F}^{\overline{xy}, \overline{xy}}$  value at the same location in Fig. 8(a).

Now, we look at the projected  $\alpha^2 \mathbf{F}$  for  $\delta E_F = -0.205$  eV. As shown in Fig. 8(b), the total  $\alpha^2 \mathbf{F}$  decreases for  $\delta E_F = -0.205$  eV comparing with  $\delta E_F = -0.055$  eV. However, for the optical modes (modes with energy bigger than 45 meV), and for  $\delta E_F = -0.205$ , the  $\alpha^2 \mathbf{F}^{\overline{xy}, \overline{xy}}$  corresponding to the phonons with in-plane displacements is enhanced in comparison with that for  $\delta E_F = -0.055$  eV. This is true in particular for the lower edge of the optical phonon spectrum marked by an arrow in Fig. 8(c), as there is a large peak composed of the phonons with in-plane displacement character, there is a sizable  $\alpha^2 \mathbf{F}^{\overline{xy}, \overline{xy}}$  for  $\delta E_F = -0.205$  at the same location in phonon energy axis in comparison with  $\alpha^2 \mathbf{F}^{\overline{xy}, \overline{xy}}$  for  $\delta E_F = -0.055$  eV. This feature could be partially attributed to the projected DOS in Fig. 2, where the total DOS is projected into  $p_x + p_y$  and  $p_z$  orbitals. By moving the  $E_F$  into the valence states the contribution of states with  $p_z$  character decreases and the contribution of states with  $p_x + p_y$  character increases. While the former results in reduced the coupling of electronic states with the phonons with major out-of-plane character, the latter results in an enhanced coupling of the electronic states to the phonons with in-plane character. However, the  $\alpha^2 \mathbf{F}^{\overline{xy}, \overline{xy}}$  behaves differently for the phonon energies below 30 meV. In this case the  $\alpha^2 \mathbf{F}^{\overline{xy}, \overline{xy}}$  of the  $\delta E_F = -0.205$  is even smaller than that of  $\delta E_F = -0.055$ . Hence, the argument regarding the enhancement of  $\alpha^2 \mathbf{F}^{\overline{xy}, \overline{xy}}$  for  $\delta E_F = -0.205$  and for phonon energies larger than 45 meV does not hold for phonon energies less than 30 meV.

We have discussed total  $\alpha^2 \mathbf{F}$  so far and we have not considered the band anisotropy, in case when we increase  $|\delta E_F|$  into the valence band states, the Fermi energy intersects with more than one energy band. To clarify the effects of band anisotropy, we plot the projection of the  $\alpha^2 \mathbf{F}$  in Fig. 9 for two different bands at the largest examined Fermi shift,  $\delta E_F = -0.205$  eV. The bands are marked by number 4 and 5 and are labeled by red and green colors, respectively, in the band structure shown in Fig. 1. As seen in Fig. 9, the  $\alpha^2 \mathbf{F}_{55}$  (related to band 5) is almost identical to that of the total  $\alpha^2 \mathbf{F}$ . Furthermore, the  $\alpha^2 \mathbf{F}_{44}$  (related to band 4) is very small in compari-

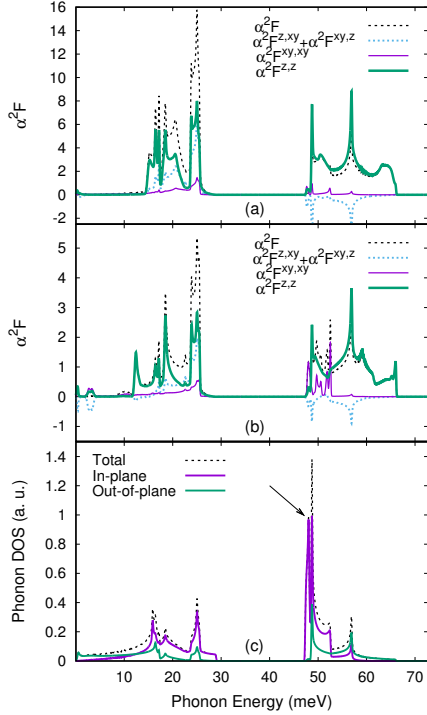


Figure 8. (Color online) (a) and (b) Projected  $\alpha^2 \mathbf{F}$  for  $\delta E_F = -0.055$  and  $\delta E_F = -0.205$  eV respectively, (c) Projected phonon DOS. The electrons couple to the deformations which are induced the out-of-plane displacements of the phonons. In the presence of the phonons with considerable out-of-plane character is a quantity to acquire sizable  $\alpha^2 \mathbf{F}$ .

son to  $\alpha^2 \mathbf{F}_{55}$ , where the corresponding projected  $\lambda$  reads  $\lambda_{55} = 2.37$  and  $\lambda_{44} = 0.12$ . This could be further understood by noticing that  $N_4(0) \ll N_5(0)$ . The smallness of the  $\alpha^2 \mathbf{F}_{44}$  is even more pronounced for a smaller  $|\delta E_F|$  due to the vanishing  $N_4(0)$  (not shown here). Therefore, in particular for the actual calculations regarding estimation of  $T_c$ , we only consider band 5 and we neglect the effects of band 4 and its coupling to band 5.

In order to calculate the energy gap, we do need to calculate the Green's function on the real frequency axis using the analytical continuation [44–46]. The superconducting energy gap can be defined as the energy difference between the ground state of the superconductor and the energy of the lowest quasi-particle excitation [47]. Furthermore, the effective energy gap in superconductors can be measured in microwave absorption experiments.

We are just interested in the critical temperature, which is also obtained by the zeroth of the energy gap along the imaginary frequency. By using the self-energy decomposition, the gap function,  $\Delta(i\omega_n)$  is defined as  $\Delta(i\omega_n) = \phi(i\omega_n)/Z(i\omega_n) = \tilde{\Sigma}_{12}(i\omega_n)/Z(i\omega_n)$ .

Having calculated the  $\alpha^2 \mathbf{F}_{55}$  which is almost identical to total  $\alpha^2 \mathbf{F}$  for all examined  $\delta E_F$  (for example see Fig. 9, we solve the isotropic Eliashberg equations

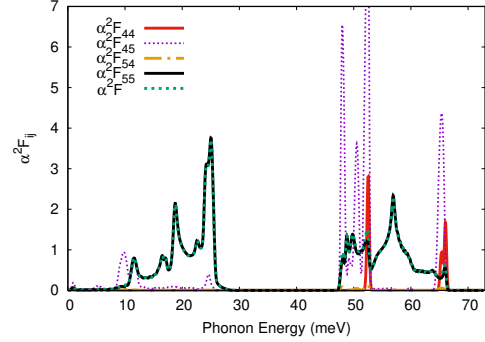


Figure 9. (Color online) Band projected  $\alpha^2 \mathbf{F}$  for  $200 \times 200$   $k$ - and  $q$ - meshes with Gaussian broadenings  $\sigma = 0.01$  eV and  $\delta E_F = -0.205$  eV. Notice that band 5 has a major contribution in the  $\alpha^2 \mathbf{F}$ .

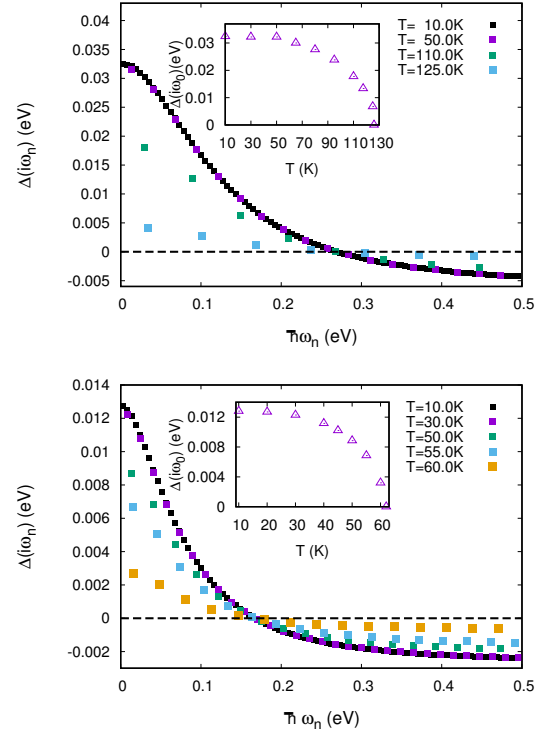


Figure 10. (Color online) Superconducting energy gap within a constant DOS approximation for different temperatures with  $\mu_c^* = 0.1$  at (top)  $\delta E_F = -0.02$  and (bottom)  $\delta E_F = -0.205$  eV in the first-order self-energy approximation. The dashed-dotted line is given as a guide to the eye to determine  $T_c$ .

for different values of the Fermi energy shifts, namely,  $\delta E_F = -0.02, -0.055, -0.105, -0.155$  and  $-0.205$  eV.

In the following we solve Eliashberg equations within different approaches discussed in the text and are compared to each other. We consider, namely Migdal-Eliashberg + constant DOS approximation (Eqs. (34), called ConsDOS), Migdal-Eliashberg + variable DOS ap-

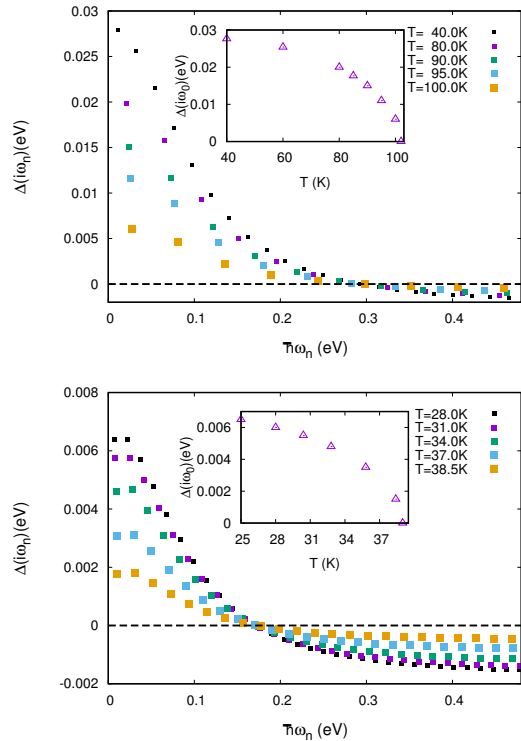


Figure 11. (Color online) Superconducting energy gap, including the vertex corrections and variable DOS approximation for different temperatures with  $\mu_c^* = 0.1$  at (top)  $\delta E_F = -0.02$  and (bottom)  $\delta E_F = -0.205$  eV. The dashed-dotted line is given as a guide to the eye to determine  $T_c$ .

proximation (Eqs. (35), (9) and (13) called VarDOS) and VarDOS + vertex corrections (the second-order diagram is included through Eqs. (38-41), Eqs. (9) and (13) called Vertex). For the sake of completeness, we estimate the  $T_c$  using the Allen-Dyns modified McMillan equation [48], where the critical temperature is given by  $T_c = \frac{\omega_{in}}{1.2} \exp\left[-\frac{1.04(1+\lambda)}{\lambda - \mu_c^*(1+0.62\lambda)}\right]$  where  $\omega_{in}$  is the logarithmical averaged frequency. Hereafter, we set  $\mu_c^* = 0.1$ . Vanishing the gap function  $\Delta(i\omega)$  is the criteria for finding the  $T_c$ .

In Fig. 10 we illustrate the variations of the  $\Delta(i\omega)$  for different temperatures and for two different shifts at  $\delta E_F = -0.02$  and  $-0.205$  eV within ConsDOS approach. Furthermore, in Fig. 11 the same plot is shown for  $\delta E_F = -0.02$  and  $-0.205$  eV, by employing Vertex approach. The reduction of the energy gap as temperature attain to the critical temperature can be taken as an indication that the charge carriers have a kind of a collective nature. That is, the charge carriers must consist of at least two things which are bound together, and the binding energy is weakening as temperature attain the critical temperature. Above the critical temperature, such collections do not exist, and normal resistivity prevails.

The calculated  $T_c$  for different  $\delta E_F$  is presented in Ta-

ble I which is our main results in this paper. Furthermore, in Table I the  $T_c$  is estimated and compared by using different approaches mentioned before. As seen in the Table I, generally speaking, while Allen-Dynes approach acquires the smallest estimate of the value of the  $T_c$  for all cases, the ConsDOS approximation overestimates the value of  $T_c$  in comparison with the VarDOS approach. The discrepancy between the ConstDOS and VarDOS is larger for  $\delta E_F$  which are located in the proximity to the apex of the DOS, where the variations of the DOS is large. For a larger shift of  $E_F$  to lower energies, the disagreement between ConsDOS and VarDOS approximations becomes smaller. The role of the vertex correction over VarDOS is non-trivially depends on the structure of the energy dispersion around the Fermi energy. Apparently, the vertex corrections are constructive to the value of  $T_c$  for  $E_F$  near the peak of the DOS, namely  $\delta E_F = -0.02$  and  $-0.055$  eV. However, the vertex correction is detrimental to  $T_c$  for the shifts away from the peak of the DOS. To further explore the ef-

$\delta E_F$	$T_c$ (Vertex)	$T_c$ (VarDOS)	$T_c$ (ConstDOS)	Allen-Dynes
-0.02	103	88	126	62
-0.055	98	88	131	64
-0.105	62	82	89	56
-0.155	43	72	72	50
-0.205	39	60	61	45

Table I. Superconductive critical temperature,  $T_c$ , in units of Kelvin for different  $E_F$  shifts and approximations. Notice, we set  $\mu_c^* = 0.1$  and the vertex corrections are included only for the electron-phonon part. The corresponding hole densities for mentioning  $\delta E_F$  are  $5.0 \times 10^{13}$ ,  $1.5 \times 10^{14}$ ,  $2.4 \times 10^{14}$ ,  $3.1 \times 10^{14}$  and  $3.8 \times 10^{14}$  cm $^{-2}$ , respectively.

fect of the vertex correction, for  $\delta E_F = -0.02$  eV, we plot in Fig. 12(a) and (b) the superconducting gap and mass renormalization at  $T = 80K$  respectively, where the VarDOS solution is compared with that based on the Vertex approach. Obviously, the superconducting gap for the vertex corrected one is larger than that obtained in the VarDOS solution, however, the Vertex approach acquires smaller mass renormalization in comparison with that calculated in the VarDOS approach. This observation, is the signature of achieving larger  $T_c$  with smaller effective  $\lambda$  through inclusion of vertex corrections [49].

#### IV. CONCLUSION

In conclusion, we have investigated a possible superconductivity of hole doped BLP. Owing to the mutual presence of nearly flat band near the VBM together with a breaking of  $\sigma_h$  symmetry in BLP, a larger electron-phonon interaction appears, upon the hole doping system. By projecting the  $\alpha^2\mathbf{F}$  into different phonon deformations, it is revealed that the out-of-plane displacement of the phonons have the largest contribution to electron-phonon interactions. For optical phonons, the contribu-

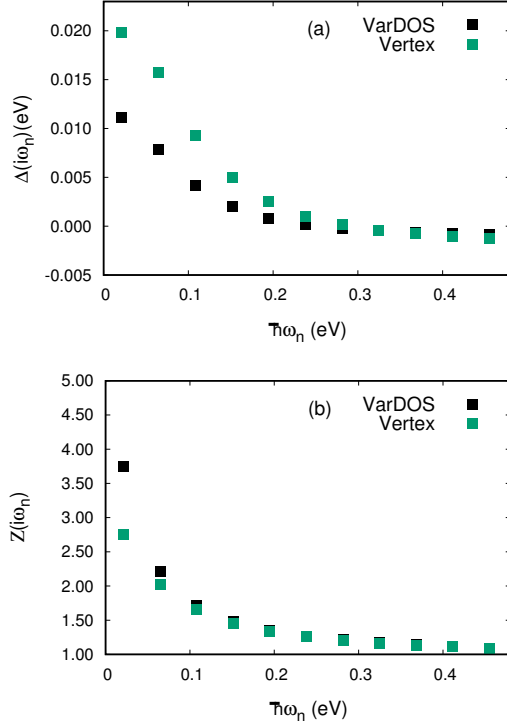


Figure 12. (Color online) (a) Superconducting energy gap and (b) mass renormalization function for  $\delta E_F = -0.02$  eV and  $T = 80$  K comparing two approaches, VarDOS and Vertex approximations.

tion of the in-plane displacements are increased upon furthering  $\delta E_F$  into VBM states, where the electronic band structure near the Fermi surface acquires larger  $p_x + p_y$  character, leading to an enhanced coupling of the electrons to the modes with larger in-plane displacements. We have further examined different approaches calculating  $T_c$  of the BLP for different shifts of  $E_F$ . The brief description of the approaches we have used is as follows: (i) Allen-Dynes formula, (ii) the first-order self-energy diagram (Migdal-Eliashberg) within assumption of a constant DOS at  $E_F$  (called ConstDOS) (iv) Considering the first-order self-energy diagram (Migdal-Eliashberg) by solving full DOS variations (called VarDOS) and (vi) assuming the  $\mathbf{k}$  averaged second-order diagram over the VarDOS approach (called Vertex).

Our calculations, summarized in Table I, show that for all  $\delta E_F$ , Allen-Dynes formula estimates smaller  $T_c$  in comparison with the other approaches. The ConstDOS overestimates  $T_c$  in comparison to the VarDOS approach which the disagreement between the two approaches appear to be smaller for a larger  $\delta E_F$  below VBM. The effect of the Vertex differs based on the  $\delta E_F$ . While the vertex correction enhances  $T_c$  for  $\delta E_F = -0.02$  and  $-0.055$  eV, it is detrimental to a larger examined  $\delta E_F$ .

We have shown in this work that the high superconducting critical temperature occurs for a hole doped blue phosphorene ranging from 100 to 40K by considering the

hole densities between  $5 \times 10^{13}$  to  $3.8 \times 10^{14}$   $\text{cm}^{-2}$  and our prediction should be verified by current experiments.

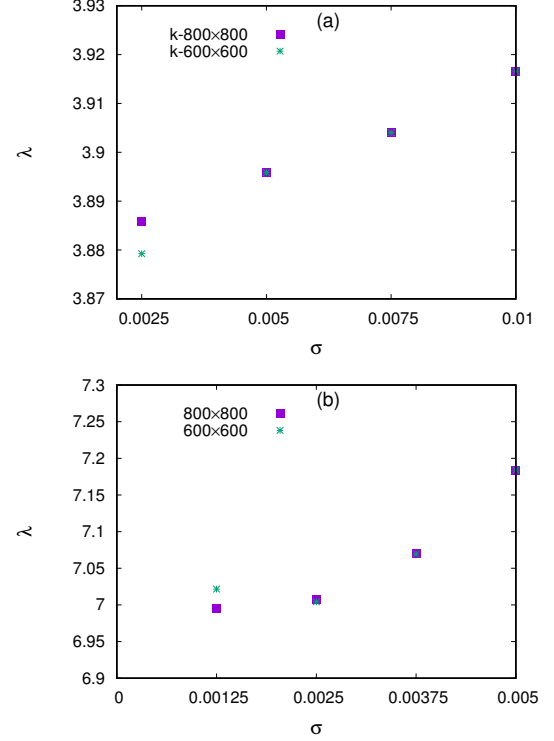


Figure 13. (Color online) (a) Total unit-less electron-phonon coupling  $\lambda$  for  $\delta E_F = -0.055$  eV as a function of Gaussian broadening  $\sigma$  for two different fine  $k$ -mesh. (b) the same as plot (a) but for  $\delta E_F = -0.105$  eV.

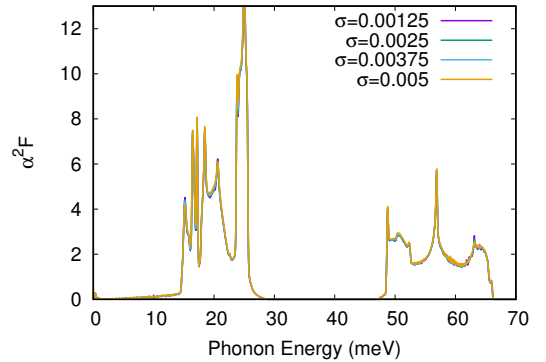


Figure 14. (Color online) (a) Total  $\alpha^2\mathbf{F}$  for  $800 \times 800$  fine  $k$ - and  $200 \times 200$  fine  $q$ - meshes as a function of electronic Gaussian broadening  $\sigma$  for  $\sigma_{ph} = 0.1$  and  $\delta E_F = -0.055$  eV.



## V. ACKNOWLEDGEMENT

We would like to thank M. Vozmediano, F. Guinea and D. Daghero for fruitful discussions. This work is partially supported by the Iran Science Elites Federation grant.

### Appendix A: Appendix

The electron-phonon matrix elements are defined as,

$$g_{\mathbf{k}i,\mathbf{k}'j}^{\nu\sigma} = \left( \frac{\hbar}{2\omega_{\mathbf{q},\nu}} \right)^{1/2} \langle \psi_{\mathbf{k}i\sigma} | \Delta^{\mathbf{q}\nu} V_{\mathbf{K}\mathbf{S}} | \psi_{\mathbf{k}'j\sigma} \rangle. \quad (\text{A1})$$

with  $\mathbf{q} = \mathbf{k}' - \mathbf{k}$ ,  $\Delta^{\mathbf{q}\nu} V_{\mathbf{K}\mathbf{S}} = \sum_{s\kappa} \frac{\partial V_{\mathbf{K}\mathbf{S}}}{\partial \mathbf{u}_{s\kappa}^{\mathbf{q}\nu}} \mathbf{u}_{s\kappa}^{\mathbf{q}\nu}$  and  $\mathbf{k}$  is an electron wave vector,  $\nu$  is the index of the phonon mode which contributes to the scattering of the electrons,  $\mathbf{q}$  is the phonon wave vector,  $\Delta^{\mathbf{q}\nu} V_{\mathbf{K}\mathbf{S}}$  is the potential owing to the displacement pattern of the phonon mode  $\nu$  and  $\frac{\partial V_{\mathbf{K}\mathbf{S}}}{\partial \mathbf{u}_{s\kappa}^{\mathbf{q}\nu}}$  is the potential difference due to a displacement of  $\mathbf{u}_{s\kappa}^{\mathbf{q}\nu}$ . Here,  $s$  is the index of atoms in the unit-cell,  $\kappa = \bar{x}, \bar{y}, \bar{z}$  is the Cartesian direction index, displacement vector  $\mathbf{u}_s^{\mathbf{q}\nu}$  is mass renormalized polarization vector, i.e.  $\mathbf{u}_s^{\mathbf{q}\nu} = \frac{1}{\sqrt{M_s}} \mathbf{e}_s^{\mathbf{q}\nu}$ , where vector  $\mathbf{e}_s^{\mathbf{q}\nu}$  is the eigenvector of the dynamical matrix [25]. For the illustrative purposes, we define a Cartesian projected electron-phonon coupling as,

$$g_{\mathbf{k}i,\mathbf{k}'j}^{\nu,\kappa} = \left( \frac{\hbar}{2\omega_{\mathbf{q},\nu}} \right)^{1/2} \langle \psi_{i\mathbf{k}} | \Delta_{\kappa}^{\mathbf{q}\nu} V_{\mathbf{K}\mathbf{S}} | \psi_{j,\mathbf{k}'} \rangle. \quad (\text{A2})$$

### Appendix B: Appendix

The different quantities i. e. DOS,  $\alpha^2\mathbf{F}$  and  $\lambda$  depend on electronic mesh size  $N_k$  and electronic Gaussian broadening  $\sigma$ . We are interested in the limit  $N_k \rightarrow \infty$  and  $\sigma \rightarrow 0$  and this is also true for phononic  $q$ -mesh size and phononic Gaussian broadening  $\sigma_{ph}$  as well. Due to the presence of a double delta summation over  $k$ -mesh in the evaluation of  $\lambda$  and  $\alpha^2\mathbf{F}$ , the convergence of  $\lambda$  and  $\alpha^2\mathbf{F}$  as a function of  $\sigma$  and  $N_k \times N_k$  is difficult. Therefore, by using a  $200 \times 200$   $q$ -mesh and  $\sigma_{ph} = 0.1$  meV, we show in which range of  $N_k$  and  $\sigma$  the above mentioned quantities are insensitive to the value of the  $N_k$  and  $\sigma$ . To this end, in Fig. 13 the total unit-less electron-phonon coupling  $\lambda$  is depicted as function of  $N_k$  and  $\sigma$ . The numerical result shows more fluctuation as a function of  $\sigma$  for  $\delta E_F = -0.055$  eV due to its vicinity to the peak of the DOS. Therefore, results are more stable for the smaller value of  $\sigma$ . Moreover, it is obvious that for the applied range of  $\sigma$  shown in Fig. 13, the  $\lambda$  is almost converged as a function of mesh-size.

In Fig. 14, total  $\alpha^2\mathbf{F}$  is shown for different values of  $\sigma$  at  $\delta E_F = 0.055$  eV. As it is clear from the figure,  $\alpha^2\mathbf{F}$  is almost insensitive to the  $\sigma$ .

- 
- [1] Y. Guo, Science **306**, 1915 (2004); D. Eom, S. Qin, M. Y. Chou, and C. K. Shih, Phys. Rev. Lett. **96**, 027005 (2006); S. Qin, J. Kim, Q. Niu, and C. K. Shih, Science **324**, 1314 (2009); T. Zhang, et al. Nat. Phys. **6**, 104 (2010); N. Reyren, et al. Science **317**, 1196 (2007); A. Gozar, et al. Nature (London) **455**, 782 (2008); D. Jiang, et al. Nat. Commun. **5**, 5708 (2014); Y. Cao, et al. Nano Lett. **15**, 4914 (2015); X. Xi, et al. Nat. Nanotechnol. **10**, 765 (2015); J. T. Ye, et al. Science **338**, 1193 (2012); D. Costanzo, S. Jo, H. Berger, and A. F. Morpurgo, Nat. Nanotechnol. **11**, 339 (2016); Y. Saito, T. Nojima and Y. Iwasa, Nature Reviews Materials **2**, 1 (2017).
- [2] J. J. Bardeen, L. N. Cooper, J. R. Schrieffer, Phys. Rev. **108**, 1175 (1957); **106**, 162 (1957).
- [3] H. Liu, A. T. Neal, Z. Zhu, Z. Luo, X. Xu, D. Tománek, and P. D. Ye, ACS Nano **8**, 4033 (2014); X. Ling, H. Wang, S. Huang, F. Xi, and M. S. Dresselhaus, PNAS **115**, 4523 (2015).
- [4] M. Wu, H. Fu, L. Zhou, K. Yao, and X. C. Zeng, Nano Lett. **15**, 3557 (2015).
- [5] J. Ribeiro-Soares, R. M. Almeida, L. G. Cançado, M. S. Dresselhaus, and A. Jorio, Phys. Rev. B **91**, 205421 (2015).
- [6] Z. Zhu and D. Tománek, Phys. Rev. Lett. **112**, 176802 (2014).
- [7] Y. Aierken, D. Cakir, C. Sevik, and F. M. Peeters, Phys. Rev. B **92**, 081408(R) (2015).
- [8] J. L. Zhang, S. Zhao, C. Han, Z. Wang, S. Zhong, S. Sun, R. Guo, X. Zhou, C. D. Gu, K. D. Yuan, Z. Li, and W. Chen, Nano Lett. **16**, 4903 (2016).
- [9] B. Liao, J. Zhou, B. Qiu, M. S. Dresselhaus, and G. Chen, Phys. Rev. B **91**, 235419 (2015).
- [10] A. Sanna, A. V. Fedorov, N. I. Verbitskiy, J. Fink, C. Krellner, L. Petaccia, A. Chikina, D. Y. Usachov, A. Grüneis and G. Profeta, 2D Materials **3**, 025031 (2016).
- [11] R. Zhang, J. Waters, A. K. Geim, and I. V. Grigorieva, Nat. Commun. **8**, 15035 (2017).
- [12] Jun-Jie Zhang and Shuai Dong, 2D Materials **3**(3), 035006 (2016).
- [13] C.-H. Park, L. Yang, Y.-W. Son, M. L. Cohen, and S. G. Louie, Nat. Phys. **4**, 213 (2008); R. Nandkishore, L. S. Levitov and A. V. Chubukov, Nat. Phys. **8**, 158 (2012).
- [14] M. B. Ludbrook, et al. Proc. Natl Acad. Sci. USA **112**, 11795 (2015); S. Ichinokura, K. Sugawara, A. Takayama, T. Takahashi, and S. Hasegawa, ACS Nano **10**, 2761 (2016).
- [15] G. Profeta, M. Calandra, F. Mauri Nature Physics **8**, 131–134 (2012).
- [16] A. Di Bernardo, O. Millo, M. Barbone, H. Alpern, Y. Kalcheim, U. Sassi, w, A.K. Ott, D. De Fazio, D. Yoon,

- M. Amado, A.C. Ferrari, J. Linder and J.W.A. Robinson, Nat. Commun. DOI: 10.1038/ncomms14024 (2017).
- [17] K. Ueno, et al. Nat. Mater. **7**, 855 (2008); J. T. Ye, et al. Nat. Mater. **9**, 125 (2010); W. Choi, N. Choudhary, G. H. Han, J. Park, D. Akinwande, and Y. H. Lee, Materials today, **20**, 116 (2017); Tong Zhang, Peng Cheng, Wen-Juan Li, Yu-Jie Sun, Guang Wang, Xie-Gang Zhu, Ke He, Lili Wang, Xucun Ma, Xi Chen, Yayu Wang, Ying Liu, Hai-Qing Lin, Jin-Feng Jia, and Qi-Kun Xue, Nat. Phys. **6**, 104 (2010).
- [18] J. L. Mañes, Phys. Rev. B **76**, 045430 (2007).
- [19] M. V. Fischetti and W. G. Vandenberghe, Phys. Rev. B **93**, 155413 (2016).
- [20] L. Boeri, G. B. Bachelet, M. Giantomassi, and O. K. Andersen, Phys. Rev. B **76**, 064510 (2007).
- [21] M. Calandra, and F. Mauri, Phys. Rev. B **74**, 094507 (2006).
- [22] J.-J. Zhang and S. Dong, 2D Materials **3**, 035006 (2016).
- [23] A. B. Migdal, Sov. Phys. JETP **34**(7), 996 (1958) [Zh. Eksp. Teor. Fiz. **34**, 1438 (1958)].
- [24] G. M. Eliashberg, Sov. Phys. JETP **11**, 696 (1960) [Zh. Eksp. Teor. Fiz. **38**, 966 (1960)].
- [25] S. Baroni, S. de Gironcoli, A. Dal Corso, and P. Giannozzi, Rev. Mod. Phys. **73**, 515 (2001).
- [26] P. Giannozzi, et. al., J. Phys. Condens. Matter **21**, 395502 (2009).
- [27] J. P. Perdew, K. Burke, and M. Ernzerhof, Phys. Rev. Lett. **77**, 3865 (1996).
- [28] F. Giustino, M. L. Cohen, and S. G. Louie, Phys. Rev. B **76**, 165108 (2007).
- [29] S. Poncé, E.R. Margine, C. Verdi and F. Giustino, Computer Physics Communications **209**, 116 (2016).
- [30] A. A. Mostofi, J. R. Yates, Y.-S. Lee, I. Souza, D. Vanderbilt, N. Marzari, Computer Physics Communications **178**, 685 (2008); **185**, 2221 (2017).
- [31] M. Elahi, K. Khaliji, S. M. Tabatabaei, M. Pourfath, R. Asgari, Phys. Rev. B **91**, 115412 (2015).
- [32] P. Giannozzi, S. deGironcoli, P. Pavone and S. Baroni, Phys. Rev. B. **43** 7231 (1991).
- [33] Y. Nambu, Phys. Rev. **117**, 648 (1960); M. Tinkham *Introduction to Superconductivity*( MacGraw-Hill, New York, 1975).
- [34] P. B. Allen and B. Mitrovic, Solid State Physics vol **37**, ed H Ehrenreich, F Seitz and D Turnbull (New York: Academic).
- [35] E. J. Nicol, J. P. Carbotte, Phys. Rev. B. **71** 054501 (2005).
- [36] Giovanni A. C. Ummarino eds. E. Pavarini, E. Koch, and U. Schollwöck *Emergent Phenomena in Correlated Matter Modeling and Simulation*, Vol **3**, (Verlag des Forschungszentrum Jülich, 2013) ISBN 978-3-89336-884-6
- [37] D. J. Scalapino, J. R. Schrieffer, and J. W. Wilkins, Phys. Rev. **148** 263 (1966).
- [38] J. R. Schrieffer, *Theory of Superconductivity* (W.A. Benjamin, New York, 1964).
- [39] P. Morel and P. W. Anderson, Phys. Rev. **125**, 1263 (1962).
- [40] N. Bogoliubov, V. Tolmachev, and D. Sirkov, *The Theory of Superconductivity, edited by N. Bogoliubov* (Gordon and Breach, New York, 1962).
- [41] F. Marsiglio, J. Low Temp. Phys. **87**, 659 (1992).
- [42] J. Bauer, J. E. Han and O. Gunnarsson, Phys. Rev. B **87**, 054507 (2013).
- [43] E. Cappelluti and L. Pietronero, Phys. Rev. B **53**, 932 (1996).
- [44] H. J. Vidberg and J. W. Serene, J. Low Temp. Phys. **29**, 179 (1977).
- [45] C. R. Leavens and D. S. Ritchie, Solid State Commun. **53**, 137 (1985).
- [46] F. Marsiglio, M. Schossmann, and J. P. Carbotte, Phys. Rev. B **37**, 4965 (1988).
- [47] M. Tinkham, *Introduction to superconductivity* (McGraw-Hill, New York (1975)).
- [48] P. B. Allen and R. C. Dynes, Phys. Rev. B **12**, 905 (1975).
- [49] C. Grimaldi, L. Pietronero, and S. Strassler, Phys. Rev. B **52**, 10530 (1995).